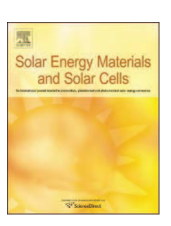
EI SEVIER

Contents lists available at ScienceDirect

Solar Energy Materials & Solar Cells

journal homepage: www.elsevier.com/locate/solmat



Solvent vapor annealing of oriented PbI₂ films for improved crystallization of perovskite films in the air



Hao Xiong^a, Giovanni DeLuca^b, Yichuan Rui^c, Yaogang Li^a, Elsa Reichmanis^{b,d,*}, Qinghong Zhang^{a,**}, Hongzhi Wang^{a,**}

- ^a State Key Laboratory for Modification of Chemical Fibers and Polymer Materials, College of Materials Science and Engineering, Donghua University, Shanghai 201620, PR China
- ^b School of Chemistry and Biochemistry, Georgia Institute of Technology, 901 Atlantic Drive, Atlanta, GA 30332, United States
- ^c College of Chemistry and Chemical Engineering, Shanghai University of Engineering Science, Shanghai 201620, PR China
- ^d School of Material Science and Engineering, Georgia Institute of Technology, 771 Ferst Drive NW, Atlanta, GA 30332, United States

ARTICLE INFO

Keywords: CH₃NH₃PbI₃ film Solvent annealing Large area crystallization Ambient stability Power conversion efficiency

ABSTRACT

The photovoltaic performance of perovskite solar cells is extremely dependent on the crystallization and morphology of the perovskite film, which are affected by the deposition method. Here, we demonstrate a simple approach to form a microporous PbI_2 film, with subsequent conversion to a compact, highly crystalline perovskite film. The PbI_2 and corresponding perovskite films were further probed by two-dimensional X-ray diffraction. The resultant perovskite exhibited improved photovoltaic performance under ambient conditions with about 50% humidity. The PbI_2 microporous structure was formed by exchanging residual DMSO with DMF vapor in the PbI_2 film, which facilitated contact with the methylammonium iodide (MAI) solution. The process resulted in the formation of compact, smooth, pinhole-free perovskite films having no residual PbI_2 . Solar cells fabricated using this methodology exhibited power conversion efficiencies over 16% with negligible photocurrent hysteresis.

1. Introduction

Organic-inorganic halide perovskite solar cells (PSCs) are now a top candidate for high-performance and low-cost thin film photovoltaics, owing to their excellent optical and electronic properties including high absorption coefficient [1–3], high electron-hole diffusion length [4,5], and superior power conversion efficiency (PCE) [6,7]. Methylammonium lead halide (CH₃NH₃PbX₃, MAPbX₃) is the most commonly used perovskite for PSC applications [8,9]. The first PSCs fabricated using MAPbI₃ and MAPbBr₃ as a sensitizer in a liquid-electrolyte-based dye-sensitized solar cells delivered a modest PCE of 3.8%[10]. Recently, a high PCE of 22.1%, certified by the National Renewable Energy Laboratory, was achieved [11]. This efficiency surpasses many other photovoltaic technology candidates [12,13].

The crystallinity and morphology of perovskite films are known to be crucial factors in the fabrication of high-efficiency devices [14]. Significant research efforts have been devoted to the design and processing of perovskite active layers, including approaches such as one-step solution spin-coating [15], vacuum vapor deposition [8], and two-step sequential deposition process [16]. The goal is to prepare compact, smooth

perovskite films with large crystalline grains. Whichever method is used, it is evident that optimizing the crystallization and grain growth conditions is critical to enhance device performance.

Park et al. reported an efficient method for preparing high efficiency perovskite solar cells under high relative humidity [14]. In their research, both substrate and PbI₂ temperature were key factors that controlled perovskite film morphology, which determined the final efficiency of the perovskite device. Precise control of temperature and humidity is difficult, but in the absence of requisite control, resultant perovskite films were not smooth, leading to interface defects between the perovskite and hole transport layers. Kelly [17] and his coworkers explored the effect of relative humidity on crystal growth, and found that perovskite crystallite size increased with increasing humidity; however, the perovskite films prepared under varying humidity conditions were not uniform and compact.

To improve the perovskite grain size, many researchers post-modified perovskite films by solvent annealing in a controlled environment [18,19]. Lau et al. optimized a solvent annealing method to improve crystallization of perovskite films and obtained an efficiency of over 13% [20]. Though post-solvent annealing can increase the perovskite crystallinity, excessive

 $\textit{E-mail addresses:} \ elsa. reichmanis @ chbe. gatech. edu (E. Reichmanis), \ zhangqh @ dhu. edu. cn (Q. Zhang), \ wanghz @ dhu. edu. cn (H. Wang).$

^{*} Corresponding author at: School of Chemistry and Biochemistry, Georgia Institute of Technology, 901 Atlantic Drive, Atlanta, GA 30332, United States.

^{**} Corresponding authors.

residual solvent is harmful to device performance. To avoid the problem mentioned above, several researchers modified the morphology of PbI $_2$, immediately obtaining uniform perovskite films. For instance, Han et al. first prepared compact amorphous PbI $_2$ for dipping deposition, however, the compact perovskite films were comprised of grains that were only around 200 nm in size [21]. Zhang et al. pretreated PbI $_2$ with Hexamethylphosphoric triamide(HMPA) , further reducing the interfacial contact between the perovskite film and TiO $_2$ layer [22]. Gong and his collaborators designed mesoporous PbI $_2$ scaffold for high performance planar perovskite solar cells, thereby obtaining a highly-crystalline perovskite film [23]. Though these results are attractive, preparation of large grain-size crystalline perovskite films in the ambient environment is still under exploration.

Inspired by solvent post-annealing, we demonstrate a straightforward method to form a high quality, oriented, crystallized PbI₂ film using a vapor post-annealing approach. The PbI₂ film subsequently affords a compact, large grain size, pinhole-free CH₃NH₃PbI₃ film under humid ambient conditions. It was found that the highly-crystalline perovskite films can significantly improve device performance and stability under humid ambient conditions.

2. Experimental section

2.1. Materials and reagents

Unless stated otherwise, all materials were purchased from Sinopharm Chemical Reagent Co., Ltd. and used as received. CH_3NH_3I and Spiro-MeOTAD (2,2',7,7'-tetrakis[N,N-di(4-methoxyphenyl)amine)–9, 9'-spirobifluorene, purity \geq 99.5%) were purchased from Xi'an Polymer Light Technology Corp. The TiO₂ paste (NJU-SR) was purchased from Kunshan Sunlaite New Energy Co., Ltd. FTO glass ($14~\Omega_{\square}^{-1}$) was purchased from Nippon Sheet Glass Co., Ltd.

2.2. CH₃NH₃PbI₃ film fabrication

The perovskite films were fabricated using a sequential deposition process. PbI2 (462 mg) was dissolved in anhydrous DMF or DMSO at 70 °C, to form a 1 M PbI₂/DMF or PbI₂/DMSO solution. The PbI₂/ DMF solution was deposited onto a FTO glass substrate by spin coating at 3000 rpm for 30 s, and the resultant film was then annealed for 10 min at 70 °C in the ambient to afford dense PbI₂ (d-PbI₂). The PbI₂/ DMSO solutions were spin-coated onto the substrates at a spin speed of $3000\,\mathrm{rpm}$ for $30\,\mathrm{s},$ followed by annealing for $10\,\mathrm{min}$ at $70\,\mathrm{^oC}.$ The PbI₂/DMSO based substrates were divided into two groups. One group formed amorphous PbI2 (a-PbI2). The other group was left on top of the hot plate at 70 °C for 10 min and covered by a glass petri dish. DMF solvent (20 µl) was introduced to the edge of the petri dish during the thermal-annealing process. This allowed the DMF vapor to diffuse under the edge of the petri dish and into the surrounding space above the PbI2 coated substrate and make contact with the PbI2 film. The DMF vapor was expected to be able to penetrate into the compact amorphous PbI2 film and promote the growth of PbI2 crystals, forming microporous PbI₂ (m-PbI₂).

 $\rm CH_3NH_3I$ dissolved in 2-propanol (10 mg/mL) at 80 °C was loaded onto d-PbI $_2$ coated, a-PbI $_2$ coated and m-PbI $_2$ coated substrate where it remained undisturbed for 20 s (loading time), The substrate was then spun at 4000 rpm for 30 s and annealed at 110 °C for 10 min, forming the dark perovskite layer which called sample 1, sample 2, and sample 3, respectively. The operation was carried out under humid ambient conditions.

2.3. Device fabrication

Solar cells having a mesoporous structure were prepared [7]. The FTO glass substrates (2.5 cm×2.5 cm) were sequentially washed through an ultrasonic treatment in detergent, acetone, ethanol and

deionized water, and treated in O2 plasma (DT-01, Suzhou Omega Machinery Electronic Technology Co., Ltd.). A thin layer of compact anatase TiO2 was formed through spin-coating using a mixed solution of titanium source on the clean substrates at 2000 rpm for 30 s, followed by a sintering process in furnace at 500 °C for 2 h. The mixed solution of titanium source was prepared as follows. Tetrabutyltitanate (850 µl) and diethanolamine (210 µl) were dissolved in ethanol (2.625 mL) under vigorous stirring for 1 h. Then 1.25 mL ethanol and 45 µl deionized water were added into the solution under vigorous stirring for 24 h. The mesoporous TiO2 layer was deposited by spin coating an unfiltered (2:7) TiO₂ paste: ethanol solution at 4000 rpm for 30 s and annealed at 500 °C for 30 min. After the perovskite films formed, a volume of 25 ul of spiroOMeTAD solution (80 mg/mL in chlorobenzene) was spin-coated onto the prepared perovskite film at 4000 rpm for 30 s. Finally, the devices were coated with a gold electrode 80 nm in thickness by evaporation through an aperture mask in a vacuum chamber. The active area of perovskite device is 0.16 cm².

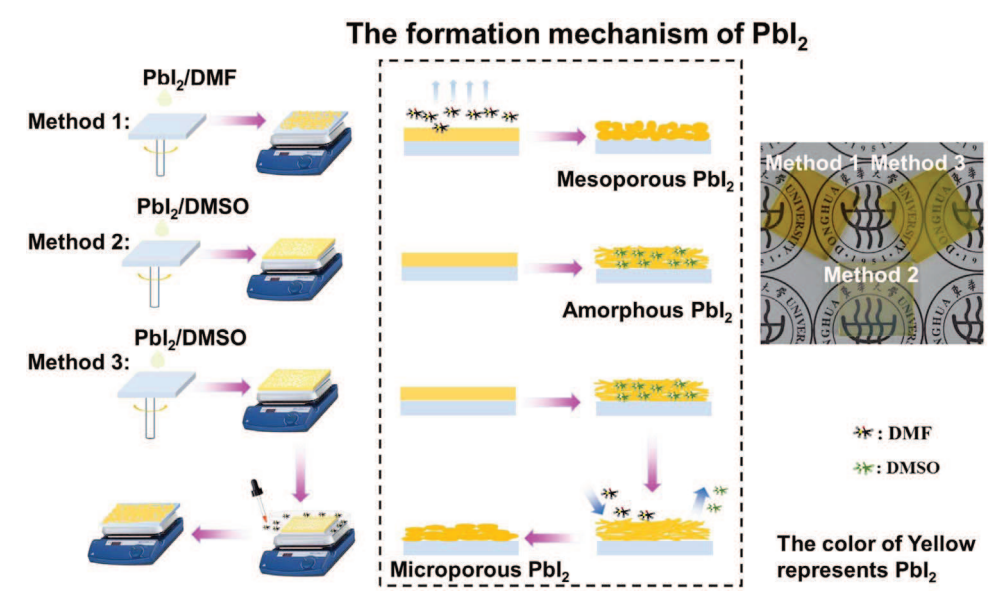
2.4. Characterization

The perovskite film was identified by one-dimensional X-ray diffraction (1D XRD) (Model D/max 2550 V, Rigaku Co. Tokyo, Japan) by using Cu Kα (λ=1.5406 Å) radiation. Two-dimensional wide-angle X-ray diffraction (WAXD) analysis was conducted using a Bruker D8 Discover GADDS X-ray Diffractometer operating at 40 kV and 40 mA, Cu Ka radiation. The morphology of the resultant perovskite film was observed by using field-emission scanning electron microscopy (FESEM, Model S-4800, Hitachi, Japan). Tapping mode atomic force microscopy (AFM) imaging was carried out using a Multimode NanoScope IV system (Veeco, Santa Barbara, CA) at a scanning range of 2 µm and a scanning speed of 3.001 Hz. Steady-state photoluminescence (PL) spectra were acquired with a FLS920 transient optical spectrometer (Edinburgh Instruments, UK). The photocurrent density-voltage (J-V) curves of the PSCs were performed by a Keithley model 2400 source measure unit. A solar simulator (Model 96160 Newport Co., USA) equipped with a 300 W Xenon lamp was used as a light source, where the light intensity was adjusted using an NRELcalibrated Si solar cell with KG-1 filter for approximating the AM 1.5 G one sun light intensity. The cell performance parameters, including short-circuit current density (Jsc), open-circuit voltage (Voc), fill factor $(FF=P_{max}/(J_{sc}V_{oc}))$, and photoelectron conversion efficiency (h (%) = $J_{sc}^*V_{oc}^*FF/total$ incident energy×100), were measured and calculated from the J-V characteristics. The incident-photon-to-current conversion efficiency (IPCE) spectra were measured as a function of the wavelength from 350 to 800 nm using a specially designed IPCE system (Newport Co., USA). Solar cell characterization and storage were carried out in ambient room conditions without encapsulation.

3. Results and discussion

High-quality perovskite films with no voids in the active layer is a key requirement for making high efficiency perovskite solar cells. However, perovskite films prepared in ambient conditions are poor, especially using a solvent method when the humidity is greater than 40% [16], which derives from the propensity of traditional PbI $_2$ structures to absorb water molecules. We optimized the preparation conditions of PbI $_2$ films, and further prepared compact, pinhole-free perovskite films in ambient conditions.

On the basis of detailed investigations of perovskite film growth, a model shown schematically in Fig. 1 was proposed. As the films were placed in a closed space, the solvent vapor could condense on the PbI $_2$ film surface. Simultaneously, the high substrate temperature could lead to solvent re-evaporation, where a simple dynamic near-equilibrium may exist [20]. It is well known that a rapidly crystalized, layered and dense PbI $_2$ film can be obtained under DMF vapor using the traditional method. Alternatively, using DMSO as the solvent for the PbI $_2$



 $\textbf{Fig. 1.} \ \text{schematic diagram for preparing three types of } PbI_2 \ \text{film and corresponding optical photographs}.$

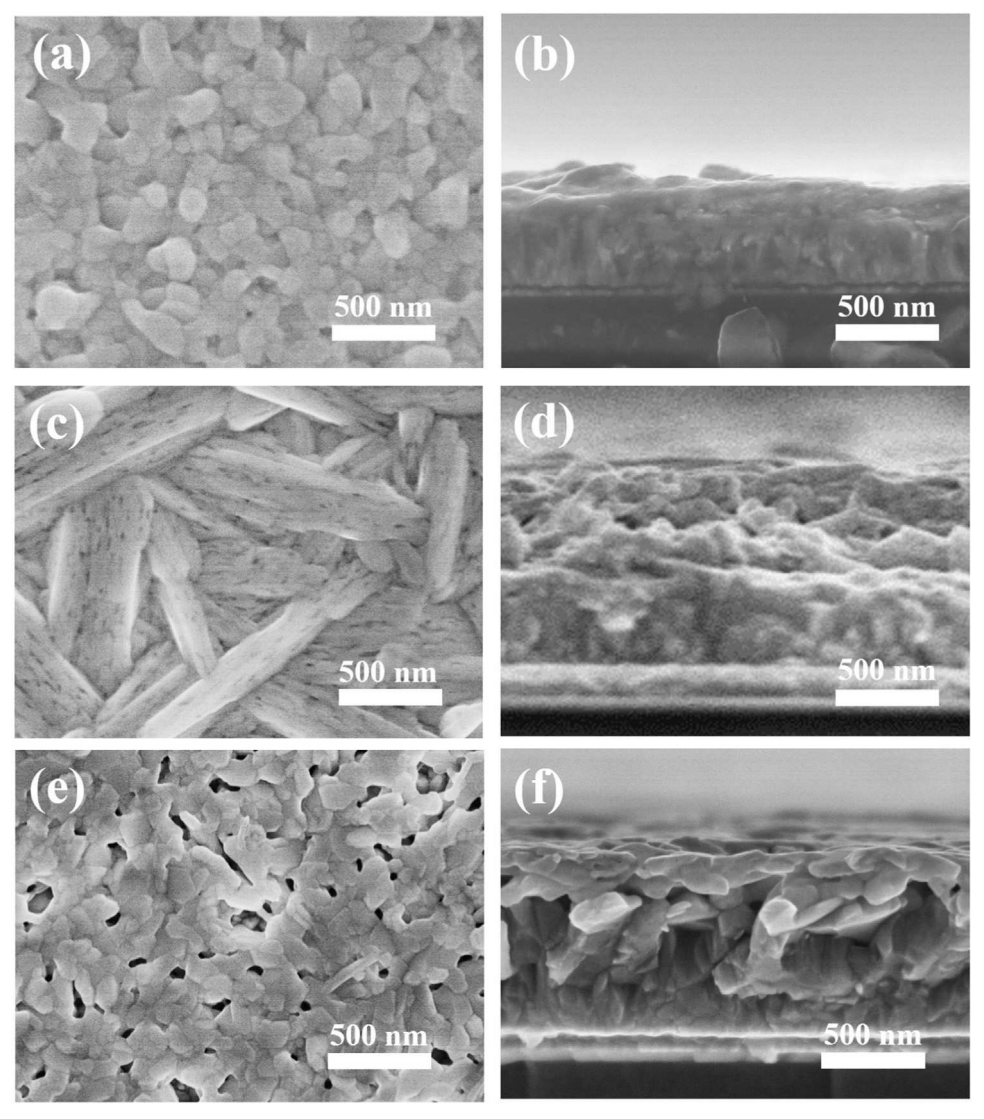


Fig. 2. Surface (left row) and Cross-sectional (right row) FE-SEM image of PbI2 films (top row) sample 1(a)(b), sample 2(c)(d) and sample 3(e)(f).

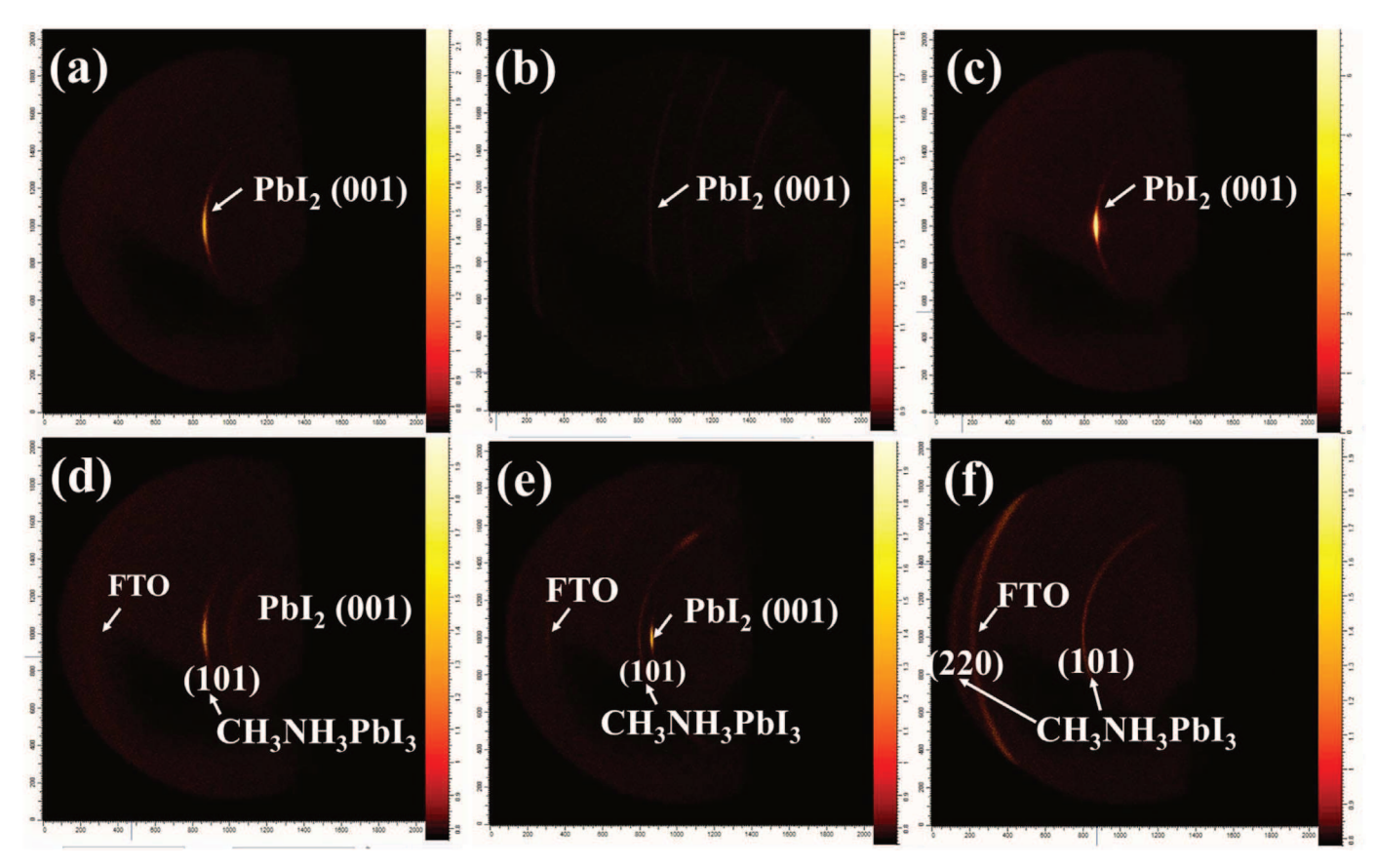


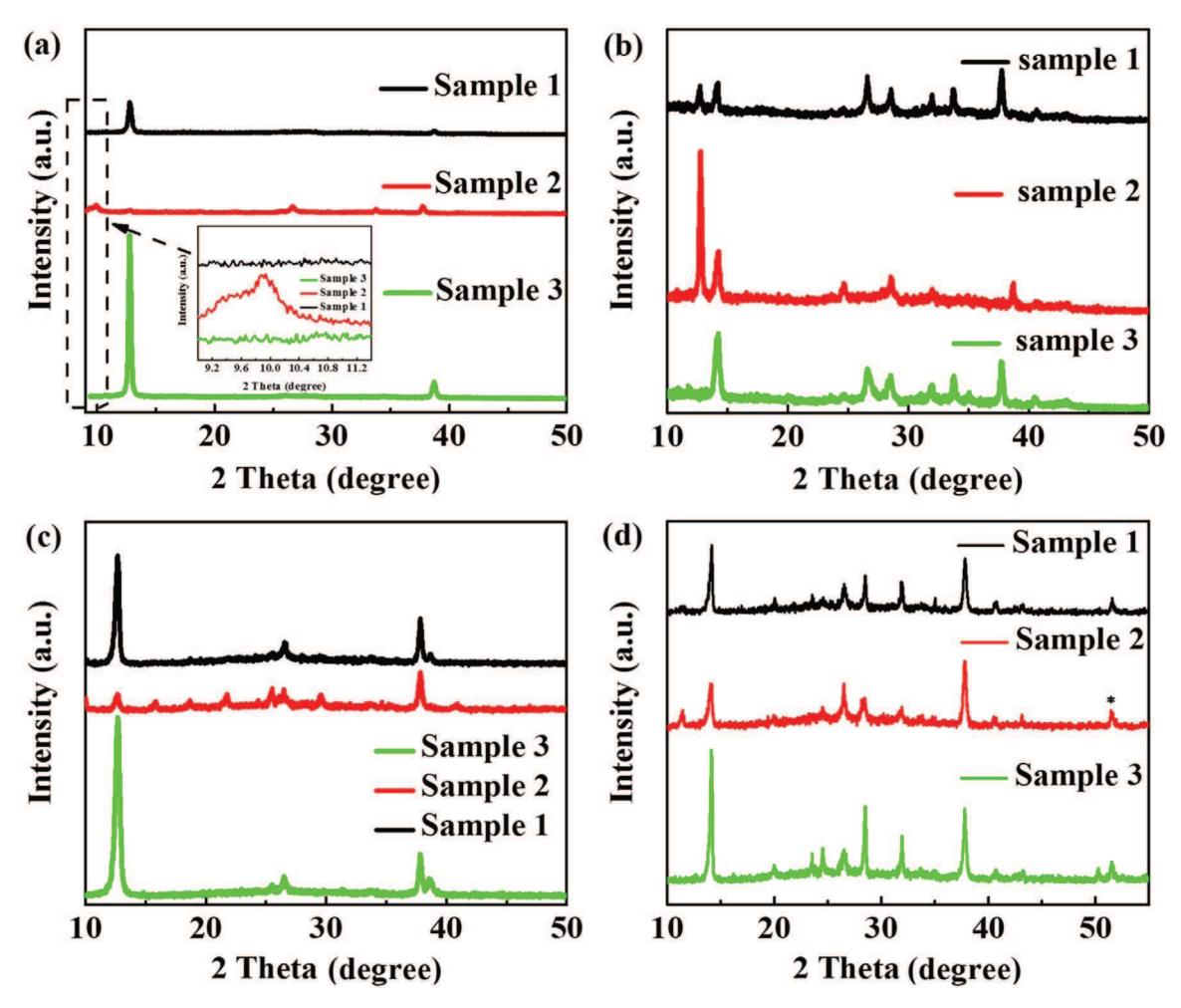
Fig. 3. Two-dimensional WAXD pattern (covered from 20 =5° to 20=20°) of PbI2 from sample 1 (a), sample 2 (b), sample 3 (c) and corresponding perovskite films (d-f).

precursor solution, an amorphous $PbI_2/DMSO$ intermediate is expected to form. Through annealing at 70 °C for several minutes, DMF molecules can infiltrate the layer and thereby substitute residual DMSO in the film, leading to PbI_2 recrystallization. The exchange between DMF and DMSO forms small pores in the PbI_2 films: PbI_2 film morphology and composition will be discussed later.

Fig. 2(a)–(f) depicts FE-SEM images of d-PbI₂, a-PbI₂ and m-PbI₂. Under ambient conditions, d-PbI₂ formed a dense layer (Fig. 2(a)), while a-PbI₂ presented a compact, amorphous surface due to the formation of the PbI₂•DMSO intermediate (Fig. 2(b)) and m-PbI₂ exhibited a microporous structure. Fig. s1 shows the pore size distribution for d-PbI₂, a-PbI₂ and m-PbI₂ film, which are calculated from the FE-SEM images. The pore sizes of the m-PbI₂ film are bigger than the two other films. Notably, the pore sizes of the d-PbI₂ film are negligible.

Though d-PbI2 can easily interact with CH3NH3I solution via the dipping method [24], the perovskite film that formed contained residual PbI2. On the other hand, d-PbI2 films can react with CH₃NH₃I efficiently, only requiring the infiltration of CH₃NH₃I into the interstices. However, the dense structure readily absorbs moisture. The absorbed water molecules would redissolve CH₃NH₃I, resulting in a decrease in CH₃NH₃I solution concentration, leading to formation of perovskite cuboids (Fig. 5(a)) [25]. Perovskite crystals are also generated from a-PbI2 films due to the stronger binding capacity of CH₃NH₃I vs. DMSO molecules with Pb²⁺, resulting in homogeneous, perovskite films comprised of small crystals (Fig. 5(c)) [26]. The m-PbI₂ combines the favorable features of d-PbI₂ and a-PbI₂ films, resulting in formation of compact highly-crystalline perovskite films in ambient conditions (Fig. 5(e)). The mechanism of crystal growth can be explained by the nucleation growth of perovskite crystals [27]. During DMF solvent annealing, oriented PbI2 crystals re-formed, and then became the nucleating point upon contact with CH₃NH₃I solution.

Two-dimensional wide-angle X-ray diffraction (2D WAXD) is widely used for analysis of the structure of solid materials, such as polymer crystals, polymer fibers, thin-film materials, bulk materials and etc. [28-31]. The fractions of crystalline, mesomorphic and amorphous phases, as well as other structure parameters can be obtained directly from analysis of the images that obtain. Through 2D WAXD image analysis, oriented, mussy or amorphous phase can be determined by spots, circles or nothing in the images, respectively. The brightness in the images represents the crystallinity of film. The continuity of circles represents the reduced crystallographic orientation. Fig. 3 shows 2D WAXD patterns for PbI₂ and the corresponding perovskite films prepared from the three methods. There are strong diffraction arcs (or spots) at Bragg angles 20 =12.6° observed for d-PbI₂ and m-PbI₂, which is attributed to the (001) lattice plane. The arc width of the strongest equatorial reflection provides a strong indication of the degree of orientation within the samples. The rings observed in the WAXD data for sample 1 are indicative of the random orientation of PbI2 crystals. In contrast, the aligned PbI2 crystals show a distinctive molecular orientation, as detected by the discrete reflections in Fig. 3(c). More importantly, a-PbI₂ exhibited weak diffraction arcs at Bragg angles 2 θ =9.9°, which contributed to the PbI₂(DMSO)₂ complex [32]. To further elaborate PbI2 film diffraction data, the one-dimensional X-ray diffraction patterns were both integrated from 2D WAXD and measured by an XRD detector. Though more information with regard to the PbI2 films can be obtained from 2D WAXD, such as oriented crystallization and residual stress, the 2D and 1D XRD results are essentially the same. Fig. 4 shows 1D XRD spectra measured from the 1D detector and integrated from 2D XRD. The a-PbI₂ films shown in Fig. 4(a) have a broadened diffraction peak at 2θ =9.9°. The 1D XRD patterns of d-PbI2 and m-PbI2 in Fig. 4 show intense peaks at 2θ =12.6° (001), 25.5° (002), 38.5°(003) and 52.2° (004) corresponding to the characteristic peaks of the PbI2 layer [33]. It has been reported that PbI2 crystals deposited from DMF solvent grow in a preferential orientation along the c axis [34]. For m-PbI₂, we find that the (001) diffraction peaks increase in intensity, suggesting a



 $\textbf{Fig. 4.} \ \, \textbf{One dimensional XRD spectra of PbI}_2 \ \, \textbf{films and corresponding perovskite films integrated from Two WAXD pattern (a)(b), measured from One WAXD pattern(c)(d).} \\$

stronger degree of the PbI_2 oriented crystallinity. The diffraction peaks of the perovskite films resulting from the corresponding PbI_2 films were observed at 2θ values of 14.39° (101), 28.35° (220) and 31.93° (141) [35]. In addition, other diffraction peaks at 2θ values of 20.08° (200), 24.60° (220), 40.81° (400) were found in sample 3, which were growth in a manner that conforms to the heterogeneous growth mechanism [36]. The signature peak of PbI_2 at 12.6° was observed in sample 2 (Fig. 4(b)(d)), which was a result of the incomplete consumption of PbI_2 in ambient conditions [37].

Fig. s2(a) shows the UV–vis absorption spectra of d-PbI₂, a-PbI₂ and m-PbI₂. The highest absorption among the three alternatives is exhibited by d-PbI₂. In Fig. s2(a), m-PbI₂ shows a slight decrease in the absorbance throughout the spectrum, which can be explained by oriented PbI₂ crystal structure. The minimal absorbance observed for a-PbI₂ film is attributed to the amorphous nature of PbI₂, as demonstrated by both FE-SEM images and XRD. Fig. s2(b) presents the UV–vis absorption spectra of the resultant perovskite films. The maximum absorption was observed for sample 3 and is attributed to the larger crystallite size and better grain inter-connectivity as shown in FE-SEM image (Fig. 5).

Photoluminescence (PL) spectroscopy provides insightful information on the charge carrier extraction properties of solar cells fabricated from the three perovskite samples. ${\rm CH_3NH_3PbI_3}$ is a highly luminescent material, which means that the quenching of its PL intensity can be used as a measure of the charge extraction ability of the perovskite layer [38]. Fig. 6(a) presents the PL spectra of the samples investigated here. The perovskite PL spectra show an intense peak at 770 nm (eV), which is in good agreement with the absorbance spectra. For sample 2,

however, a blue-shift to 765 nm was observed. This change in absorbance is believed to be related to the presence of unreacted PbI₂ [39]. Additional support for the presence of PbI₂ id derived from Energy Dispersive Spectrometer (EDS) data pertaining to the measured Pb/I ratio shown in Table s1. From the data analysis, the elemental Pb content is slightly enriched in the film which supports the UV-vis analysis above. To study the dynamics of electron lifetimes between the devices, time-resolved photoluminescence (TRPL) spectroscopy was also performed. Fig. 6(b) illustrates the TRPL spectroscopic analysis of three perovskite films fabricated on FTO glass. Such measurements provide quantitative information associated with light-induced charge separation [40]. Samples 1 and 2 exhibited a time constant of te =16.76 ns, and $\tau = 22.60$ ns, respectively, whereas sample 3 exhibited a better value of τe =32.14 ns. Charge carriers possessing longer lifetimes are expected to have a lower defect concentration [41]. The higher electron lifetime is due to the low recombination rate. The increase in photocurrent density is likely to be in part related to the rapid transport rate, associated with the efficiency of charge collection.

3.1. Photovoltaic performance of perovskite solar cells

After optimizing the compact pinhole free perovskite film in ambient conditions with $\sim 50\%$ humidity, solar cells were fabricated with a device architecture of glass/FTO/compact TiO₂/mesoporous TiO₂/CH₃NH₃PbI₃/spiroOMeTAD/Au.

To ensure consistency and accuracy, several independent methods were used to investigate photovoltaic performance. Perovskite solar

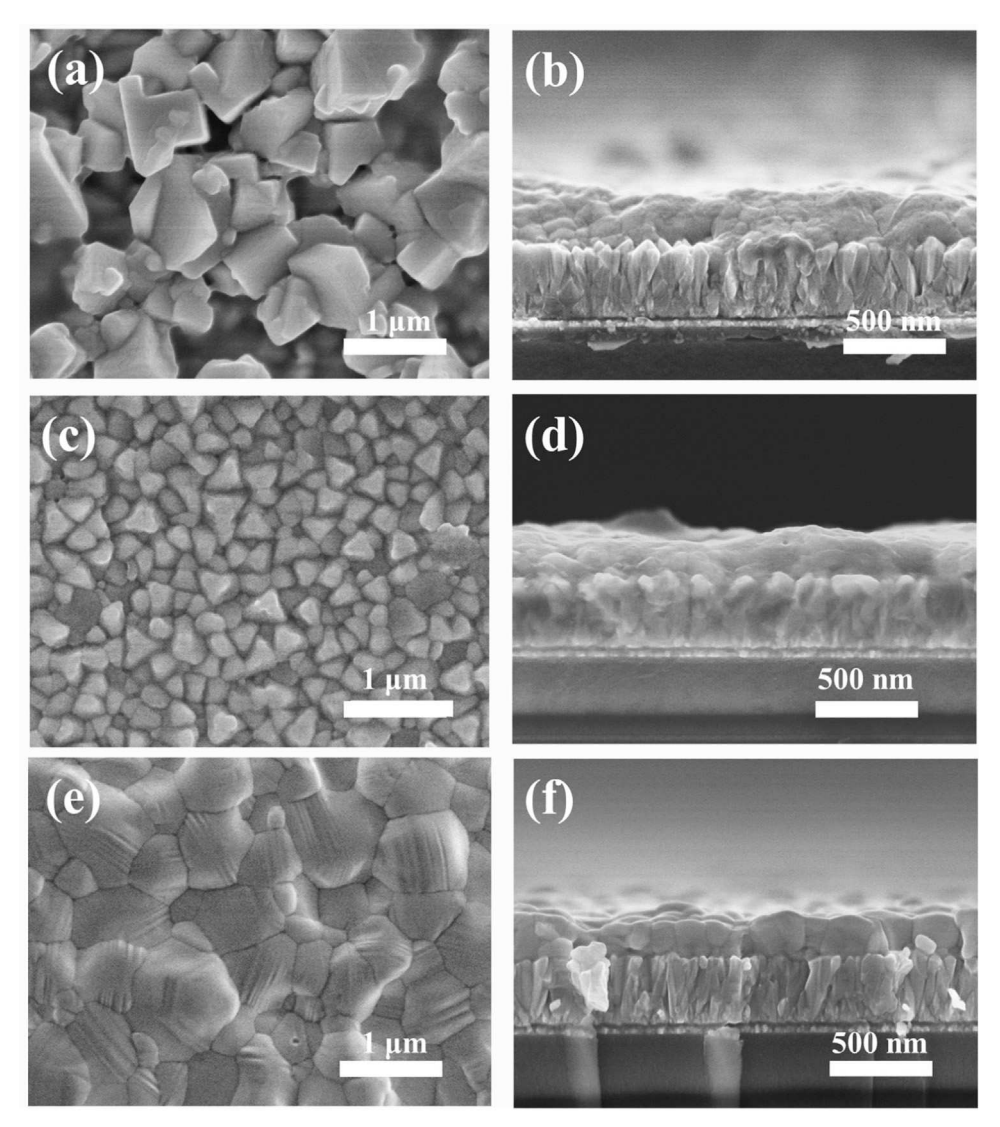


Fig. 5. Surface (left row) and Cross-sectional (right row) FE-SEM image of perovskite films sample 1(a)(b), sample 2(c)(d) and sample 3(e)(f).

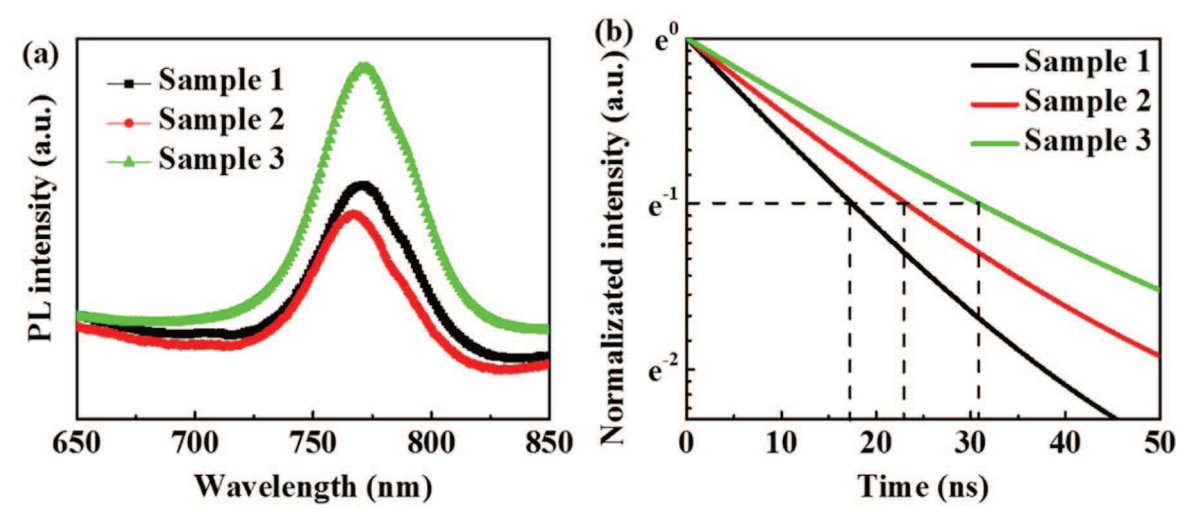


Fig. 6. (a) Photoluminescence of perovskite samples on FTO glass. (b) TRPL data for perovskite sample.

cells often exhibit hysteresis, which relates to the quality of perovskite layer [42]. Poor quality of the perovskite film will result in capacitance between the perovskite and other layers [43]. Power conversion efficiencies were determined by current-voltage characterization by sweeping the voltage from negative to positive (forward scan) and

positive to negative values (reverse scan). The $J_{\rm sc}$ of the devices was calibrated against the monochromatic incident photon-to-electron conversion efficiency. The devices were further tested under maximum power point tracking to investigate the device stability.

Fig. 7(a-c) shows the current-voltage curve of the three types of

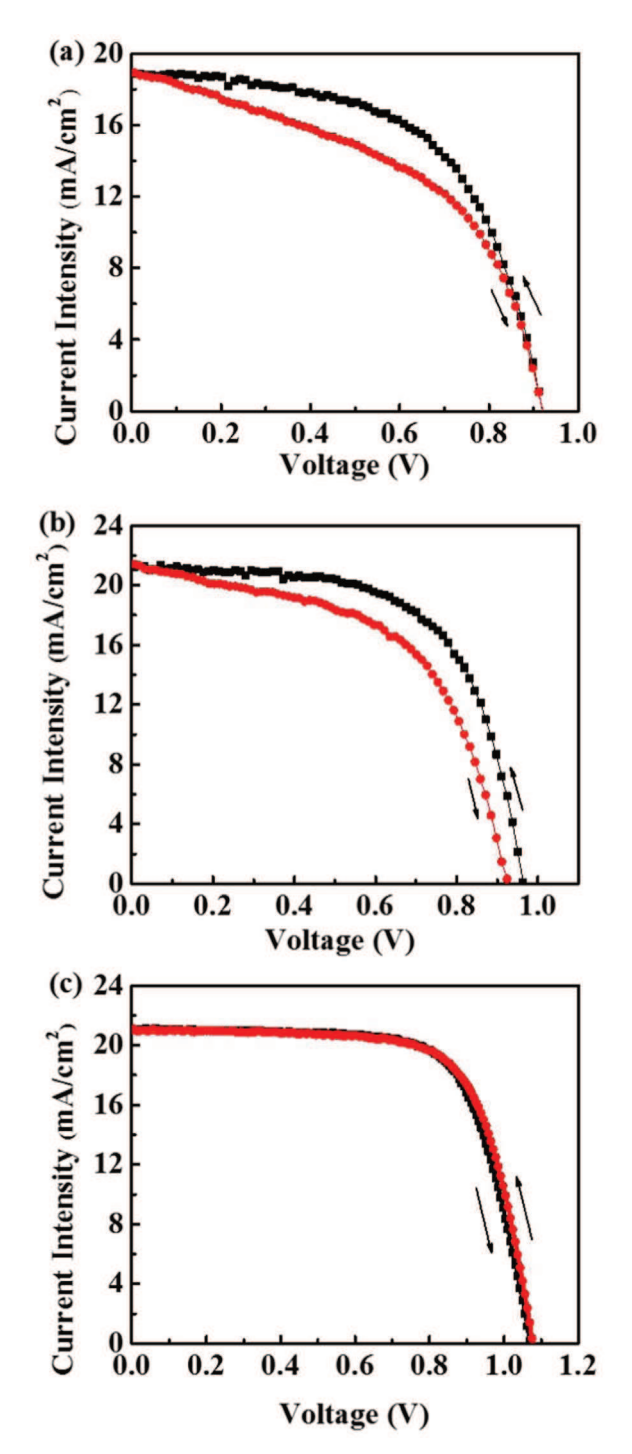


Fig. 7. J-V curves under both (black line) forward and (red line) reverse scans for best devices. (a) sample 1 (b) sample 2 (c) sample 3. (For interpretation of the references to color in this figure legend, the reader is referred to the web version of this article.)

solar cells. Cells fabricated from samples 1 and 2 exhibited significant hysteresis, while little hysteresis was observed from solar cells based on sample 3. A rough, pinhole containing perovskite film leads to capacitance between the perovskite film and other layers, following the charge-discharge taking place at the interface of the perovskite and hole transporting layers [44]. Table s2 summarizes the typical device performance based on the above-mentioned structure. For the device using sample 1 films, an efficiency of 10.06% was obtained with a $\rm V_{oc}$ of 0.92 V, $\rm J_{sc}$ of 18.93 mA/cm² and a FF of 57.79 under reverse scan. A poor efficiency of 8.50% with a $\rm V_{oc}$ of 0.92 V, $\rm J_{sc}$ of 19.01 mA/cm² and FF of 48.65 was achieved under forward scan. The devices show

significant photocurrent hysteresis, a noteworthy feature of perovskite trap states, which generate capacitance at the interfaces. Sample 2 device performance reached a medium level compared to the reference with an efficiency of 10.81% obtained from a V_{oc} of 0.92 V, J_{sc} of 21.30 mA/cm² and FF of 54.95 under forward scan, while an efficiency of 12.77% with a $V_{\rm oc}$ of 0.96 V, $J_{\rm sc}$ of 21.23 mA/cm2and a FF of 62.44 under reverse scan was achieved. As expected, devices fabricated from sample 3 films exhibited the best performance, namely a champion PCE of 16.01% with Voc of 1.08 V, Jsc of 21.02 mA/cm² and a FF of 70.67 under reverse scan. An efficiency of 15.93% with V_{oc} of 1.07 V, J_{sc} of 21.02 mA/cm² and a FF of 70.67 under forward scan was achieved. The low FF of solar cells fabricated using sample 1 films can be attributed to the rough nature of the perovskite films. It is widely believed that the FF is the key parameter associated with perovskite device performance, which may be related to carrier recombination at the interface between perovskite films and electron/hole transport layers [45]. Fig. s3 depicts the two-dimensional AFM images which reveal the overall topography of the sample 1, 2, and 3 procedures. The morphology varies significantly with sample preparation procedure, and corroborates the FE-SEM results (Fig. 5). The root mean square (rms) roughness of the three samples are 172 nm, 56.4 nm, and 39.8 nm respectively. This kind of relative decrease in rms roughness of the perovskite active layer is expected to be advantageous, because it can lead to enhanced $V_{\rm oc}$ as shown by Li et al. [46].

Fig. 8(a) shows IPCE measurement of devices with sample 1 (black line), 2 (red line) and 3 films (green line). The curves start increasing rapidly at around 770 nm, which is related to the optical absorption edge of the perovskite films [47]. Between 450 nm and 800 nm, the absorption profile of devices based on sample 1 is lower than those of sample 2 and sample 3, which may derive from fewer perovskite grains. Between 350 nm and 450 nm, the absorption of the sample 2 device decreased sharply, due to incomplete perovskite grain formation compared to the other two devices. To check the stabilization or saturation point of photocurrent in solar cells with the different perovskite formation protocols, the stabilized power output close to the maximum power point was carried out at the voltage of 0.82 V (sample 3), 0.73 V (sample 2) and 0.68 V (sample 1). The steady-state photocurrent represents the actual power output and is used to accurately characterize the device efficiency. As shown in Fig. 8(b), under simulated AM1.5 G radiation (100 mW/cm²) and bias voltage at the maximum power point, sample 3 produced a more stable output current than the other two samples, with the latter showing a diminished current over time.

Furthermore, statistical data regarding the photovoltaic parameters for the three solar cell fabrication methods are plotted in Fig. s4, where the data are obtained from 14 or more cells. Most of the parameters associated with perovskite solar cells fabricated from sample 3 were superior to those obtained from the alternate methodologies, which provides further evidence that better quality perovskite films afforded better device performance.

4. Conclusions

In summary, a low-cost and simple two-step deposition technique was developed to form microporous PbI_2 , based on post-annealed processing in ambient conditions. We investigated the effect of the crystallinity of PbI_2 films on resultant perovskite films and ultimate photovoltaic performance. A power conversion efficiency of 16.01% was achieved with devices fabricated from PbI_2 films having a mesoporous structure. The $CH_3NH_3PbI_3$ film morphology that resulted from the mesoporous precursor was very uniform as confirmed by AFM images. These results demonstrate the importance of morphology control in the PbI_2 phase for high-performance PSCs fabricated under ambient conditions. The simple technique presented here could be used to prepare large area perovskite solar cells in ambient conditions.

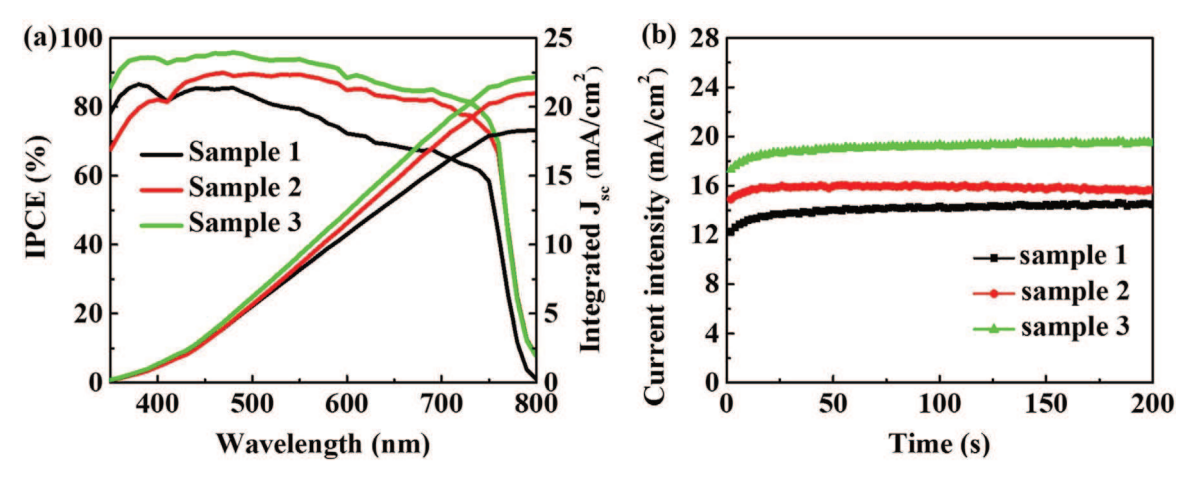


Fig. 8. (a) IPCE spectra of the devices with different perovskite films. (b) The steady-state current measured at the maximum power point for sample 1 (0.68 V), sample 2 (0.73 V) and sample 3 (0.82 V). (For interpretation of the references to color in this figure, the reader is referred to the web version of this article.).

Acknowledgments

We gratefully acknowledge the financial support by Natural Science Foundation of China (No.51572046, 51503035), The Shanghai Natural Science Foundation (15ZR1401200), the Program for Professor of Special Appointment (Eastern Scholar) at Shanghai Institutions of Higher Learning, Program of Shanghai Academic Research Leader (16XD1400100), Science and Technology Commission of Shanghai Municipality (16JC1400700), and the Program of Introducing Talents of Discipline to Universities (No.111-2-04) and the Major Program of the National Natural Science Foundation of China (51590902). GD is grateful for support from the NSF EAPSI program (OISE1613514); ER thanks the Georgia Institute of Technology for support. ER additionally appreciates support from the Brook Byers Institute for Sustainable Systems at Georgia Tech.

Appendix A. Supplementary material

Supplementary data associated with this article can be found in the online version at doi:10.1016/j.solmat.2017.03.028.

References

- [1] W.-J. Yin, J.-H. Yang, J. Kang, Y. Yan, S.-H. Wei, Halide perovskite materials for solar cells: a theoretical review, J. Mater. Chem. A 3 (2015) 8926–8942.
- [2] C. Li, X. Lu, W. Ding, L. Feng, Y. Gao, Z. Guo, Formability of ABX₃ (X= F, Cl, Br, I) Halide Perovskites, Acta Crystallogr. Sect. B Struct. Sci. 64 (2008) 702–707.
- [3] T. Baikie, Y. Fang, J.M. Kadro, M. Schreyer, F. Wei, S.G. Mhaisalkar, M. Graetzel, T.J. White, Synthesis and crystal chemistry of the hybrid perovskite (CH₃NH₃)PbI₃ for solid-state sensitised solar cell applications, J. Mater. Chem. A 1 (2013) 5628–5641.
- [4] C.C. Stoumpos, C.D. Malliakas, M.G. Kanatzidis, Semiconducting tin and lead iodide perovskites with organic cations: phase transitions, high mobilities, and near-infrared photoluminescent properties, Inorg. Chem. 52 (2013) 9019–9038.
- [5] V. D'Innocenzo, G. Grancini, M.J.P. Alcocer, A.R.S. Kandada, S.D. Stranks, M.M. Lee, G. Lanzani, H.J. Snaith, A. Petrozza, Excitons versus free charges in organo-lead tri-halide perovskites, Nat. Commun. 5 (2014) 3586.
- [6] W.S. Yang, J.H. Noh, N.J. Jeon, Y.C. Kim, S. Ryu, J. Seo, S. Il Seok, Highperformance photovoltaic perovskite layers fabricated through intramolecular exchange, Science 348 (2015) 1234–1237.
- [7] H.-S. Kim, C.-R. Lee, J.-H. Im, K.-B. Lee, T. Moehl, A. Marchioro, S.-J. Moon, R. Humphry-Baker, J.-H. Yum, J.E. Moser, M. Grätzel, N.-G. Park, Lead iodide perovskite sensitized all-solid-state submicron thin film mesoscopic solar cell with efficiency exceeding 9%, Sci. Rep. 2 (2012) 591.
- [8] M. Liu, M.B. Johnston, H.J. Snaith, Efficient planar heterojunction perovskite solar cells by vapour deposition, Nature 501 (2013) 395–398.
- [9] M.M. Lee, J. Teuscher, T. Miyasaka, T.N. Murakami, H.J. Snaith, Efficient hybrid solar cells based on *meso*-superstructured organometal halide perovskites, Science 338 (2012) 643–647.
- [10] A. Kojima, K. Teshima, Y. Shirai, T. Miyasaka, Organometal halide perovskites as visible-light sensitizers for photovoltaic cells, J. Am. Chem. Soc. 131 (2009) 6050–6051.
- [11] M. Saliba, T. Matsui, J.-Y. Seo, K. Domanski, J.-P. Correa-Baena, N. Mohammad K, S.M. Zakeeruddin, W. Tress, A. Abate, A. Hagfeldt, M. Grätzel, Cesium-containing

- triple cation perovskite solar cells: improved stability, reproducibility and high efficiency, Energy Environ. Sci. 9 (2016) 1989–1997.
- [12] Y. Wang, Y. Rui, Q. Zhang, Y. Li, H. Wang, A facile in situ synthesis route for CuInS2 Quantum-Dots/In2S3 Co-sensitized photoanodes with high photoelectric performance, ACS Appl. Mater. Interfaces 5 (2013) 11858–11864.
- [13] Y. Rui, Y. Li, Q. Zhang, H. Wang, Size-tunable TiO₂ nanorod microspheres synthesised via a one-pot solvothermal method and used as the scattering layer for dve-sensitized solar cells, Nanoscale 5 (2013) 12574.
- [14] H.-S. Ko, J.-W. Lee, N.-G. Park, 15.76% efficiency perovskite solar cells prepared under high relative humidity: importance of PbI₂ morphology in two-step deposition of CH₃NH₃PbI₃, J. Mater. Chem. A 3 (2015) 8808–8815.
- [15] M.K. Gangishetty, R.W.J. Scott, T.L. Kelly, Effect of relative humidity on crystal growth, device performance and hysteresis in planar heterojunction perovskite solar cells. Nanoscale 8 (2016) 6300–6307.
- [16] J. Yang, B.D. Siempelkamp, D. Liu, T.L. Kelly, An investigation of CH₃NH₃PbI₃ degradation rates and mechanisms in controlled humidity environments using in situ techniques, ACS Nano 9 (2015) 1955–1963.
- [17] M.K. Gangishetty, R.W.J. Scott, T.L. Kelly, Effect of relative humidity on crystal growth, device performance and hysteresis in planar heterojunction perovskite solar cells. Nanoscale 8 (2016) 6300–6307.
- [18] J. You, Y.M. Yang, Z. Hong, T.-B. Song, L. Meng, Y. Liu, C. Jiang, H. Zhou, W.-H. Chang, G. Li, Moisture assisted perovskite film growth for high performance solar cells, Appl. Phys. Lett. 105 (2014) 183902.
- [19] Z. Xiao, Q. Dong, C. Bi, Y. Shao, Y. Yuan, J. Huang, Solvent annealing of perovskite-induced crystal growth for photovoltaic-device efficiency enhancement, Adv. Mater. 26 (2014) 6503–6509.
- [20] J. Liu, C. Gao, X. He, Q. Ye, L. Ouyang, D. Zhuang, C. Liao, J. Mei, W. Lau, Improved crystallization of perovskite films by optimized solvent annealing for high efficiency solar cell, ACS Appl. Mater. Interfaces 7 (2015) 24008–24015.
- [21] Y. Wu, A. Islam, X. Yang, C. Qin, J. Liu, K. Zhang, W. Peng, L. Han, Retarding the crystallization of PbI $_2$ for highly reproducible planar-structured perovskite solar cells via sequential deposition, Energy Environ. Sci. 7 (2014) 2934.
- [22] Y. Zhang, P. Gao, E. Oveisi, Y. Lee, Q. Jeangros, G. Grancini, S. Paek, Y. Feng, M.K. Nazeeruddin, Pbl₂—HMPA Complex Pretreatment for Highly Reproducible and Efficient CH₃NH₃Pbl₃ Perovskite Solar Cells, J. Am. Chem. Soc. 138 (2016) 14380–14387.
- [23] T. Liu, Q. Hu, J. Wu, K. Chen, L. Zhao, F. Liu, C. Wang, H. Lu, S. Jia, T. Russell, R. Zhu, Q. Gong, Mesoporous PbI₂ scaffold for high-performance planar heterojunction perovskite solar cells, Adv. Energy Mater. 6 (2015) 1614–6840.
- [24] J. Burschka, N. Pellet, S.-J. Moon, R. Humphry-Baker, P. Gao, M.K. Nazeeruddin, M. Grätzel, Sequential deposition as a route to high-performance perovskitesensitized solar cells, Nature 499 (2013) 316–319.
- [25] J.-H. Im, I.-H. Jang, N. Pellet, M. Grätzel, N.-G. Park, Growth of CH₃NH₃PbI₃ cuboids with controlled size for high-efficiency perovskite solar cells, Nat. Nanotechnol. 9 (2014) 927–932.
- [26] Y. Wu, A. Islam, X. Yang, C. Qin, J. Liu, K. Zhang, W. Peng, L. Han, Retarding the crystallization of PbI 2 for highly reproducible planar-structured perovskite solar cells via sequential deposition, Energy Environ. Sci. 7 (2014) 2934.
- [27] P. Liang, C. Liao, C. Chueh, F. Zuo, S. Williams, X. Xin, J. lin, A. Jen, Additive enhanced crystallization of solutio-processed perovskite for highly efficient planarheterojunction solar cells, Adv. Mater. 26 (2014) 3748–3754.
- [28] K. Tashiro, S. Sasaki, M. Kobayashi, Structural investigation of orthorhombic-to-hexagonal phase transition in polyethylene crystal: the experimental confirmation of the conformationally disordered structure by X-ray diffraction and infrared/Raman spectroscopic measurements, Macromolecules 29 (1996) 7460–7469.
- [29] S. Ran, X. Zong, D. Fang, B.S. Hsiao, B. Chu, R. Ross, Novel image analysis of twodimensional X-ray fiber diffraction patterns: example of a polypropylene fiber drawing study, J. Appl. Crystallogr. 33 (2000) 1031–1036.
- [30] M.J. Kory, M. Wörle, T. Weber, P. Payamyar, S.W. Van De Poll, J. Dshemuchadse, N. Trapp, A.D. Schlüter, Gram-scale synthesis of two-dimensional polymer crystals and their structure analysis by X-ray diffraction, Nat. Chem. 6 (2014) 779–784.

- [31] T. Brezesinski, J. Wang, S.H. Tolbert, B. Dunn, Ordered mesoporous [alpha]-MoO₃ with iso-oriented nanocrystalline walls for thin-film pseudocapacitors, Nat. Mater. 9 (2010) 146–151.
- [32] W. Li, J. Fan, J. Li, Y. Mai, L. Wang, Controllable Grain Morphology of Perovskite Absorber Film by Molecular Self-Assembly toward Efficient Solar Cell Exceeding 17%, 2015, pp. 10399–10405.
- [33] M. Baibarac, N. Preda, L. Mihut, I. Baltog, S. Lefrant, J.Y. Mevellec, On the optical properties of micro-and nanometric size PbI₂ particles, J. Phys. Condens. Matter 16 (2004) 2345.
- [34] S. Lee, J. Feldman, S.S. Lee, Nanoconfined Crystallization of MAPbI₃ to Probe Crystal Evolution and Stability, Cryst. Growth Des. 16 (2016) 4744–4751.
- [35] T. Oku, Crystal Structures of ${\rm CH_3NH_3PbI_3}$ and Related Perovskite Compounds Used for Solar Cells, 2015.
- [36] Y. Kumar, E. Regalado-Pérez, A.M. Ayala, N.R. Mathews, X. Mathew, Effect of heat treatment on the electrical properties of perovskite solar cells, Sol. Energy Mater. Sol. Cells 157 (2016) 10–17.
- [37] Z. Zhang, D. Wei, B. Xie, X. Yue, M. Li, D. Song, Y. Li, High reproducibility of perovskite solar cells via a complete spin-coating sequential solution deposition process, Sol. Energy 122 (2015) 97–103.
- [38] Y. Yamada, M. Endo, A. Wakamiya, Y. Kanemitsu, Spontaneous defect annihilation in CH₃NH₃PbI₃ thin films at room temperature revealed by time-resolved photoluminescence spectroscopy, J. Phys. Chem. Lett. 6 (2015) 482–486.
- [39] T.J. Jacobsson, J.-P. Correa-Baena, E. Halvani Anaraki, B. Philippe, S.D. Stranks, M.E.F. Bouduban, W. Tress, K. Schenk, J. Teuscher, J.-E. Moser, Unreacted PbI₂ as a double-edged sword for enhancing the performance of perovskite solar cells, J. Am. Chem. Soc. 138 (2016) 10331–10343.
- [40] S.S. Mali, C.S. Shim, H. Kim, P.S. Patil, C.K. Hong, In situ processed gold

- nanoparticle-embedded TiO₂ nanofibers enabling plasmonic perovskite solar cells to exceed 14% conversion efficiency, Nanoscale 8 (2016) 2664–2677.
- [41] D.W. de Quilettes, S.M. Vorpahl, S.D. Stranks, H. Nagaoka, G.E. Eperon, M.E. Ziffer, H.J. Snaith, D.S. Ginger, Impact of microstructure on local carrier lifetime in perovskite solar cells, Science 348 (2015) 683–686.
- [42] W. Tress, N. Marinova, T. Moehl, S.M. Zakeeruddin, N. Mohammad K, M. Grätzel, M.K. Nazeeruddin, M. Grätzel, Understanding the rate-dependent J–V hysteresis, slow time component, and aging in CH₃NH₃PbI₃ perovskite solar cells: the role of a compensated electric field, Energy Environ. Sci. 8 (2015) 995–1004.
- [43] C. Sun, Z. Wu, H. Yip, H. Zhang, X. Jiang, Q. Xue, Z. Hu, Z. Hu, Y. Shen, M. Wang, F. Huang, Y. Cao, Amino-functionalized conjugated polymer as an efficient electron transport layer for high-performance planar-heterojunction perovskite solar cells, Adv. Energy Mater. 6 (2016) 1501534.
- [44] M. Xiao, F. Huang, W. Huang, Y. Dkhissi, Y. Zhu, J. Etheridge, A. Gray-Weale, U. Bach, Y.-B. Cheng, L. Spiccia, A. Fast Deposition-Crystallization, Procedure for highly efficient lead iodide perovskite thin-film solar cells, Angew. Chem. Int. Ed. 53 (2014) 9898–9903.
- [45] A. Pecchia, D. Gentilini, D. Rossi, M. Auf der Maur, A. Di Carlo, Role of ferroelectric nanodomains in the transport properties of perovskite solar cells, Nano Lett. 16 (2016) 988–992.
- [46] G. Li, K.L. Ching, J.Y.L. Ho, M. Wong, H.-S. Kwok, Identifying the optimum morphology in high-performance perovskite solar cells, Adv. Energy Mater. 5 (2015) 1401775.
- [47] M.B. Price, J. Butkus, T.C. Jellicoe, A. Sadhanala, A. Briane, J.E. Halpert, K. Broch, J.M. Hodgkiss, R.H. Friend, F. Deschler, Hot-carrier cooling and photoinduced refractive index changes in organic—inorganic lead halide perovskites, Nat. Commun. 6 (2015) 8420.